

Phosphorene as a Catalyst for Highly Efficient Nonaqueous Li–Air Batteries

Lance Kavalsky,[†] Sankha Mukherjee,[†] and Chandra Veer Singh^{*,†,‡}

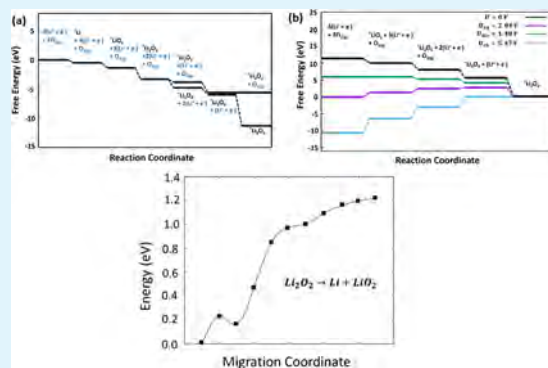
[†]Department of Materials Science and Engineering, University of Toronto, 184 College Street, Suite 140, Toronto, ON M5S 3E4, Canada

[‡]Department of Mechanical and Industrial Engineering, University of Toronto, 5 King's College Road, Toronto M5S 3G8, Canada

Supporting Information

ABSTRACT: Li–air batteries can yield exceptionally high predicted energy densities. However, for this technology to become realizable, round-trip efficiency issues and slow kinetics at the cathode require implementation of a catalyst. With design parameters not well understood and limitations on material selection, choosing an ideal catalyst is complex. In Li–air batteries, energy storage is achieved by reactions between Li and O (oxygen reduction reaction for discharge and oxygen evolution reaction for charge). Here, phosphorene is proposed as a solution through simulations of its catalytic behavior toward discharge initiated via either O₂ dissociation or Li adsorption. After obtaining intermediate geometries for both nucleation paths leading to either Li₂O₂ or 2(Li₂O), free-energy diagrams are generated to predict the promoted discharge product of Li₂O₂. Furthermore, considering a final product of Li₂O₂, the overpotentials are predicted to be 1.44 V for discharge and 2.63 V for charge. Activation barriers for the catalytic decomposition of Li₂O₂ (during charge) are found to be 1.01 eV for phosphorene versus 2.06 eV for graphene. This leads to a major difference in reaction rate up to 10¹⁷ times in favor of phosphorene. These results, complemented by electronic analysis, establish phosphorene as a promising catalyst for Li–air batteries.

KEYWORDS: DFT, Li–air battery, 2D phosphorene, catalysis, NEB, overpotential



1. INTRODUCTION

Of the next-generation energy storage systems, Li–air batteries have attracted a lot of attention as they are predicted to have much higher energy densities than alternative battery technologies. However, many issues remain before they can be realized commercially.^{1,2} About two decades ago, the first nonaqueous Li–oxygen battery system was demonstrated by K. Abraham and Jiang giving hope to its practical potential.³ One of the main drawbacks of Li–air batteries is that they currently suffer from poor round-trip efficiencies, which can be attributed to large overpotentials.¹ Overpotential is the difference in voltage between either the charging or discharging voltage and the equilibrium voltage and is a consequence of internal resistances in the cell. In addition, the discharge product can have a significant effect on the reversibility of the system, with Li₂O₂ being the preferred discharge product.⁴ Addressing the poor efficiency inherent to these cells has sparked research into solvent catalysts, redox mediators, and suitable catalysts that can contribute catalytically to both the oxygen evolution reaction (OER) and the oxygen reduction reaction (ORR), which correspond to the charge and discharge reactions, respectively.⁵ Bruce demonstrated the positive effect of introducing a catalyst to a nonaqueous system on the overpotential through a systematic comparison of a variety of different catalyst materials.⁶ However, the exact mechanisms of how the catalyst

involves itself in the reaction remain poorly understood.^{1,5} Through increased catalytic activity, the overall research aim is to improve upon the efficiency of these reactions at the cathode, thereby addressing one of the major hindrances of these batteries. Furthermore, a catalyst that can promote the formation of Li₂O₂ over Li₂O is highly desirable in terms of improving upon cyclability.⁴

Of the materials investigated so far, precious metals such as Pt and Pd have shown some of the best catalytic activities as air cathodes. Among these precious metal catalysts and glassy carbon (GC), the order of ORR activities was demonstrated to be Pd > Pt > Ru ≈ Au > GC.⁷ However, these materials are highly expensive, which limits their applicability in a commercially feasible system. Carbon materials such as doped graphene⁸ and siligraphenes⁹ have also been (theoretically) reported to exhibit excellent catalytic activity but are shown experimentally to have unwanted side reactions with the electrolyte, which decrease the cycle life.¹⁰ Thus, a search for carbon-free catalysts is underway with two-dimensional (2D) materials attracting attention^{8,9,11–16} as they have gained traction with other battery types because of their high surface-

Received: August 7, 2018

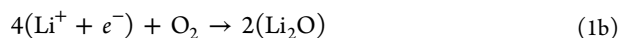
Accepted: December 6, 2018

Published: December 6, 2018

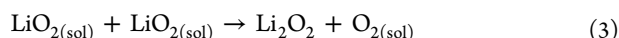
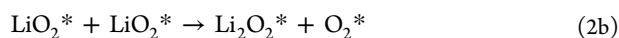
to-volume ratios and interesting electronic and mechanical properties.^{17–20}

In this continuing search for catalysts to decrease the overpotential in the cathode, phosphorene has emerged as a potential candidate for this role. Phosphorene is an exciting new material with interesting electronic properties and has already been predicted to show promise in other battery contexts such as Li-S batteries (which was also studied experimentally).²¹ On the other hand, although phosphorene has been observed to degrade in ambient air conditions, the prerequisites have been demonstrated to be exposure to light, water, and oxygen,^{22,23} with light being the main factor^{24,25} (mainly in the UV regime²⁶). Previous density functional theory (DFT) studies have predicted the necessity of the presence of at least both O₂ and H₂O for this degradation process.²⁷ However, research is being conducted into developing oxygen separation membranes to create a pure oxygen environment,^{1,28,29} and by keeping the battery in dark, pure O₂ conditions, the issue of degradation can be avoided.³⁰ In addition, much work has been conducted to further increase the stability in ambient conditions including adding protective capping layers on the surface^{31,32} and employing a heat treatment to the system.³⁰ From a practicality standpoint, phosphorene nanosheets can be fabricated from bulk red phosphorus,³³ thereby demonstrating its feasibility. Additionally, phosphorene has demonstrated excellent electrocatalytic abilities as a photocatalyst, which opens the door for its exploration in other catalytic applications.³⁴ Recently, phosphorene nanosheets were investigated experimentally for their catalytic ability toward OER and were found to have excellent activity and stability toward this reaction.³⁵ However, to our knowledge, there have not been any theoretical investigations into phosphorene for the context of Li–air batteries, leaving much room for additional insights into the fundamentals of its catalytic behavior.

It is generally agreed upon that there are two possible final discharge products that a Li–air battery cell may yield. The first stems from a two-electron reaction where the final discharge product is Li₂O₂, and the second stems from a four-electron reaction that yields 2(Li₂O)^{4,28}



Regarding (1a), after LiO₂ is formed as an intermediate, it has been proposed that the peroxide may be formed either via a surface mechanism or a solution mechanism depending on the electrolyte, which are outlined below.^{36–38}



Focusing on the surface mechanism, Li₂O₂ can be formed either via electrochemical reduction (eq 2a) or disproportionation (eq 2b),^{36,37} with the former shown to be kinetically favorable.³⁶ As done elsewhere, we have also assumed the solubility of LiO₂ in the electrolyte to be negligible as it depends on the electrolyte's donor number,³⁹ which we have used as justification for not considering eq 3. Because of these assumptions, we anticipate that the reaction path toward Li₂O₂ would proceed through this electrochemical reduction process. As the reaction progresses, the discharge product will continue to grow on the surface and

cover the cathode. This layer is not necessarily ordered. For example, in the case of CNTs doped with RuO₂ nanoparticles, the discharge product surface was found to have very poor crystallinity.⁴⁰ Therefore, in this work, we will consider electrochemical reduction as a surface mechanism to form either Li₂O₂ or 2(Li₂O).

Both reactions start with either Li adsorption or O₂ dissociation onto the substrate,⁹ and, henceforth, 2(Li₂O) and Li₄O₂, and 2(Li₂O₂) and Li₄O₄ are used interchangeably. Elsewhere, determination of the nucleation mechanism (Li adsorption or O₂ dissociation) is conducted through thermodynamic considerations alone.^{9,11,15} However, this does not consider the activation barrier for O₂ dissociation, which will effectively bottleneck this reaction. Moreover, because Li adsorption is spontaneous, we expect Li to act as a nucleation site in addition to O₂, with both processes occurring simultaneously. To explore both mechanisms, we systematically study the reactions starting with either O₂ dissociation or Li adsorption.

In this work, first-principles density functional theory (DFT) simulations were conducted to obtain estimates of the overpotentials for a nonaqueous Li–air battery using phosphorene. Additionally, DFT was used to provide predictions on the discharge product for this proposed system. As an extension to these studies, we conducted investigations into the differential charge density (DCD), charge analysis, and projected density of states (PDOS) to shed further light on the underlying chemistry of the system. Finally, the climbing-image nudged elastic band (CI-NEB) method was used to evaluate the activation barriers for removal of Li from Li₂O₂ to give an estimate of catalytic charging behavior. The purpose of this work is to not only evaluate phosphorene's potential catalytic capabilities as a cathode in Li–air batteries but also contribute to the fundamental understanding of these systems.

2. COMPUTATIONAL METHODS

The Quantum Espresso package⁴¹ was used to conduct spin-polarized DFT simulations through the projector augmented wave method.⁴² The exchange correlation was approximated using the Perdew–Burke–Ernzerhof⁴³ functional within the generalized gradient approximation. The convergence threshold for self-consistency through the DFT computations was 10^{−6} Ry. For calculations regarding atomic positions and lattice parameters of phosphorene, a kinetic energy cutoff of 60 Ry and charge density cutoff of 480 Ry were employed. Considering pristine phosphorene, a 3 × 3 supercell (36 atoms) with a vacuum of 16 Å was employed with van der Waals forces accounted for through the DFT-D2 approach.⁴⁴ Various vacuum sizes were tested to best eliminate spurious interlayer interactions (Table S2). For visualization of the structures, XCrySDen⁴¹ and VESTA⁴⁵ were utilized. When studying formation of these molecules on the phosphorene substrate, a 4 × 4 × 1 Monkhorst–Pack⁴⁶ grid was sampled in the Brillouin zone for calculation of the total energies. The adsorption energy of each of the adatoms on the substrate is calculated by

$$E_{\text{Ads,Li}_x\text{O}_y} = E_{\text{P+Li}_x\text{O}_y} - E_{\text{P}} - xE_{\text{Li}} - \frac{y}{2}E_{\text{O}_2} \quad (4)$$

where $E_{\text{P+Li}_x\text{O}_y}$ is the total energy of the system with the adsorbent attached, E_{P} is the energy of pristine phosphorene, E_{Li} is the energy per atom of Li in bulk (bcc) form, and E_{O_2} is the energy of the O₂ molecule in its ground state (triplet state). To calculate the change in internal energy when forming Li_xO_y from Li_xO_y adsorbed on the substrate, the following expression is utilized

$$\Delta E_{\text{Ads}} = E_{\text{P+Li}_x\text{O}_y} - E_{\text{P+Li}_x\text{O}_y} - (x - u)E_{\text{Li}} - \frac{y - v}{2}E_{\text{O}_2} \quad (5)$$

where E_{Li} is the energy per atom of Li in bulk form, $E_{\text{P+Li}_x\text{O}_y}$ is the total energy of the new system, and $E_{\text{P+Li}_x\text{O}_y}$ is the total energy of the old system. Only consecutive reaction steps are considered, so either $(x - u) = 1$ and $(y - v) = 0$ or $(x - u) = 0$ and $(y - v) = 2$, with $x, y \in 0, 1, 2, 3, 4$. The optimal configurations were taken to be the orientation of the adatom, which provides the lowest total energy of the system after the Broyden–Fletcher–Goldfarb–Shanno⁴⁷ algorithm was employed to variable-cell-relax the system.

As done previously for oxidation, the triplet state of oxygen (the ground state) was modeled using spin-polarized DFT, whereas for the singlet state of oxygen, the spin was restricted to avoid spin contamination.⁴⁸ Spin polarization was also implemented to accurately capture any bond breaking that may occur as the reaction proceeds.

To further illuminate the interaction between the reaction intermediates and the phosphorene substrate at the optimum configurations, differential charge density (DCD) plots are generated through the following equation

$$\Delta\rho_{\text{Ads}} = \rho_{\text{P+Li}_x\text{O}_y} - \rho_{\text{P}} - \rho_{\text{Li}_x\text{O}_y} \quad (6)$$

where $\rho_{\text{P+Li}_x\text{O}_y}$ is the charge density of the adsorbed state, ρ_{P} is the charge density of the bare substrate, and $\rho_{\text{Li}_x\text{O}_y}$ is the charge density of the isolated intermediate. These plots provide a visual representation of the charge transfer at important steps of the reaction. Additionally, Bader charge analysis is conducted to quantify the charge transfer present.⁴⁹

To predict the reaction mechanism in phosphorene, the Gibbs free energies at each step of the reaction were computed. For every optimized configuration of the intermediate adatoms, the Gibbs free energies are calculated by

$$G_{\text{Ads, Li}_x\text{O}_y} = E_{\text{Ads, Li}_x\text{O}_y} + \text{ZPE}_{\text{Li}_x\text{O}_y} - \text{TS}_{\text{Li}_x\text{O}_y} \quad (7)$$

where $\text{ZPE}_{\text{P+Li}_x\text{O}_y}$ and $\text{TS}_{\text{P+Li}_x\text{O}_y}$ are the zero-point energy and entropic effects (with the temperature set to 300 K) of the adsorbent system relative to each of their constituents, respectively. The pressure and volume contributions were assumed to be negligible under order-of-magnitude arguments used previously.⁵⁰ The configurational component of entropy was also taken to be negligible,⁵¹ leaving only vibrational considerations for entropy and zero-point energy. Moreover, the substrate was held fixed as done previously.¹¹ The vibrational modes, and thus the vibrational energies, were calculated through the finite displacement method. This method calculates the differences in energy under displacement of each constituent atom of the intermediate molecule to approximate the Hessian matrix. All atoms considered were displaced by 0.01 Å in three orthogonal directions. The magnitude of the displacement was determined via a convergence test by observing the stability of the first vibrational mode of O₂ on phosphorene at various displacement lengths (see Figure S1). The Atomic Simulation Environment⁵² was used with its built-in interface for Quantum Espresso to run these vibrational simulations. From the vibrational modes, the vibrational Helmholtz free energy is calculated using

$$F_{\text{vib}} \equiv \text{ZPE}_{\text{P+Li}_x\text{O}_y} - \text{TS}_{\text{vib, P+Li}_x\text{O}_y} \\ = \sum_i \frac{\epsilon_i}{2} + k_{\text{B}}T \ln \left(1 - \exp \left[\frac{-\epsilon_i}{k_{\text{B}}T} \right] \right) \quad (8)$$

where \hbar is the reduced Planck's constant, ϵ_i is the i th vibrational energy of the intermediate adatom, and k_{B} is the Boltzmann constant. Because of these vibrational calculations, the free-energy diagram can be generated and the overpotentials can be predicted.

Employing the climbing-image nudged elastic band (CI-NEB) method,⁵³ the activation barrier required to remove Li from Li₂O₂ was investigated in a manner similar to what has been done for Li-S batteries⁵⁴ to obtain an estimate of catalytic behavior toward charging.

3. RESULTS AND DISCUSSION

3.1. Initial Nucleation Step of Discharge Mechanism.

The first step in the reaction will be to either adsorb a Li adatom or dissociate an O₂ molecule onto the surface of phosphorene. This will behave as the nucleation site of the discharge product on the catalyst and will influence the structure of the reaction intermediates. If the reaction starts with O₂ dissociation, two Li will need to be added to form Li₂O₂. Otherwise, if the discharge mechanism starts with Li adsorption, then O₂ and another Li atom will need to be deposited to again form Li₂O₂. The addition of another formula unit will disclose whether the two-electron or four-electron reaction (eq 1a,1b) is preferred and introduce asymmetry between the discharge and charge overpotentials.⁸ In other words, additional Li and O₂ are added to the substrate, with the energies compared to determine whether another Li₂O₂ forms (Li₄O₄) or if the reaction will proceed toward 2(Li₂O).

Considering the thermodynamics of the process, the adsorption energy of Li onto the substrate was found to be -0.55 eV over the hollow site of the lattice. Elsewhere, this has been identified as the most favorable adsorption site for Li on phosphorene.^{55–57} For O₂ physisorption above the substrate, the binding energy was calculated to be -0.13 eV. However, if O₂ can dissociate over the bridge site of phosphorene, the binding energy per O atom was found to be -2.06 eV. Physisorption in this manner was predicted to be the beginning of the main oxidation path.⁴⁸

Interactivity of phosphorene with O₂ becomes an important point as it can determine whether physisorbed or chemisorbed states should be considered. The spin state of O₂ can play an important role in the dissociation process. O₂ in its ground state is a triplet state from Hund's rule, which states that when there are empty orbitals available the spins will orientate themselves to maximize multiplicity. The triplet state corresponds to the spins of the shared electrons becoming parallel, and the singlet state has the spins oriented anti-parallel. It was previously shown that instead of direct dissociation of O₂ over pristine phosphorene, which requires overcoming a barrier of 5.6 eV, there exists another possibility.⁴⁸ As an alternative, indirect dissociation can occur where an oxygen bridge is first formed, and if the O₂ transitions from a triplet to a singlet state, it can dissociate with a barrier of 0.54 eV.⁴⁸ However, the probability of this triplet-to-singlet transition was estimated to be only 0.12, which effectively bottlenecks the process.⁴⁸ For comparison, silicon has a transition probability of 0.001 eV.⁵⁸ With the combination of requiring a triplet-to-singlet transition and overcoming the 0.54 eV energy barrier, we expect dissociation to occur, but slowly. This leads to O₂ dissociation in addition to Li adsorption, providing two mechanisms of discharge growth that we anticipate will occur simultaneously. Therefore, both types of discharge product nucleation mechanisms are considered in this work.

3.1.1. Reaction Intermediate Geometries from O₂ Nucleation. To find the best geometrical configuration for each intermediate step of the reaction, the Li atom or O₂ molecule was adsorbed to the previous optimized step configuration. For example, after O₂ dissociation, a Li atom was adsorbed onto the fully relaxed substrate with the two O atoms already relaxed on the surface. Multiple initial positions of the introduced atom were taken into consideration to ensure that the preferred geometry is identified. The configuration with the most negative

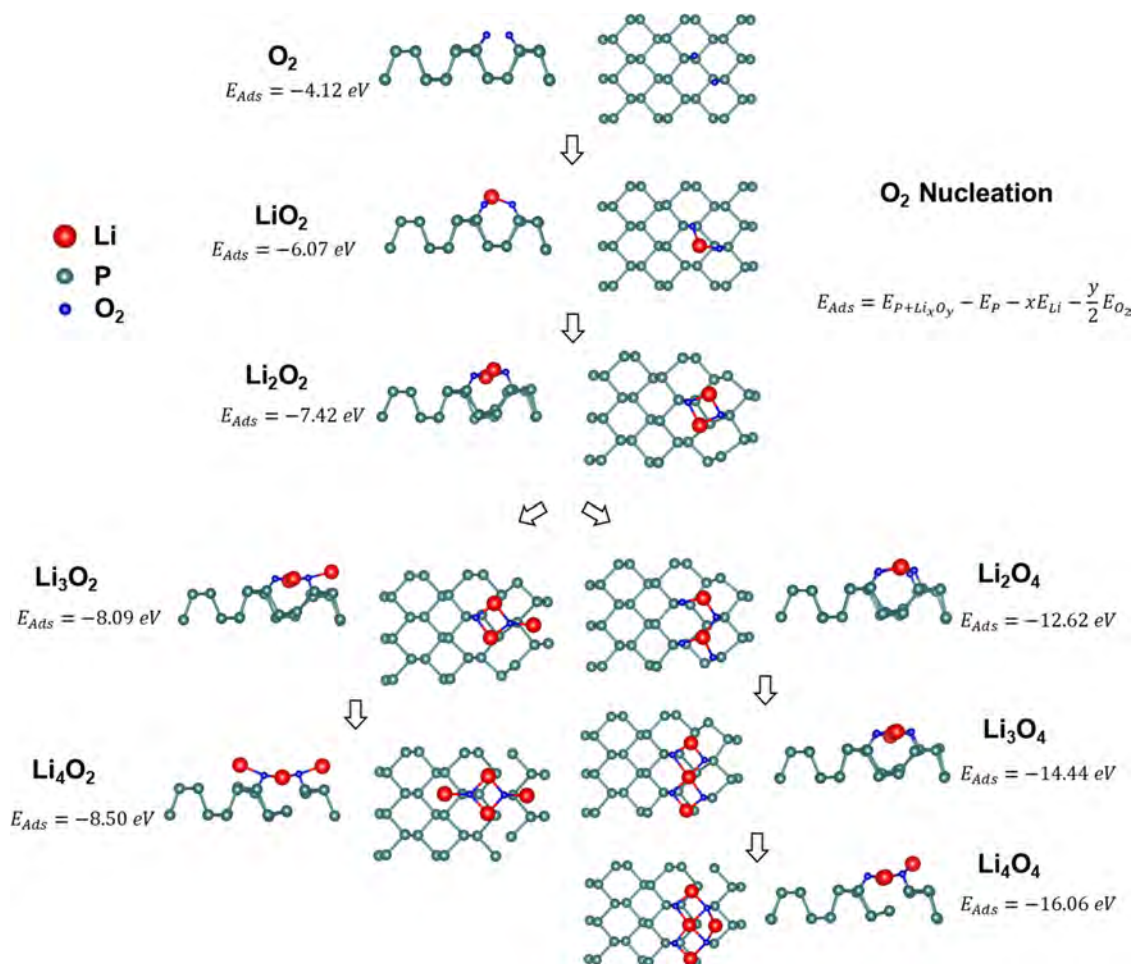


Figure 1. Optimized intermediate geometries for the reaction mechanism stemming from O_2 dissociation. Color code: green, P; blue, O; and red, Li. Atomic structures were visualized using VESTA.⁴⁵

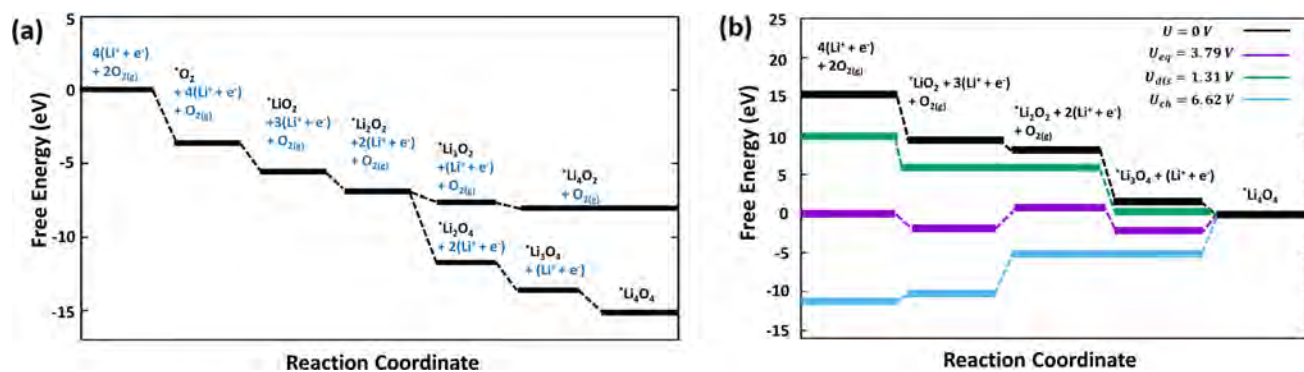


Figure 2. (a) Free-energy diagram comparing the two mechanism branches starting from O_2 dissociation and leading to either Li_4O_2 or Li_4O_4 . (b) Free-energy diagram illustrating the mechanism at different electric potentials.

binding energy (i.e., most energetically favorable) was taken to be the optimal configuration for that intermediate.

Starting with the O_2 nucleation mechanism, the next step is the addition of a Li atom to form LiO_2 . Upon relaxation, the Li atom preferred to lie over the H-site in between the dissociated oxygen molecules. On adding another Li atom to create Li_2O_2 , the new addition preferred to sit opposite to the other Li to form a flat diamondlike structure and the existing Li lowers toward the substrate (Figure 1). The geometry of this intermediate draws comparison with the equivalent molecule during the predicted ORR mechanism on silicene,¹³ siligraphenes,⁹ h-BN/Ni(111),¹⁴

and g-GeC;¹² however, a Pt/Cu alloy is not anticipated to demonstrate the same symmetry.⁵⁹ Following this step, the reaction can either take the path toward Li_4O_4 (indicating that Li_2O_2 is the promoted product) or continue to Li_4O_2 depending on the catalyst. The former refers to a continuation of the previous reactions to form a second unit of Li_2O_2 , and the latter refers to the formation of the alternative discharge product Li_4O_2 . On the track to Li_4O_2 , Li_3O_2 is expected to be formed first from adding a Li atom to Li_2O_2 . In this case, the additional Li relaxed to a position beside the diamond, forming a tail (Figure 1). Finally, the fourth Li atom preferred to lie on the opposite

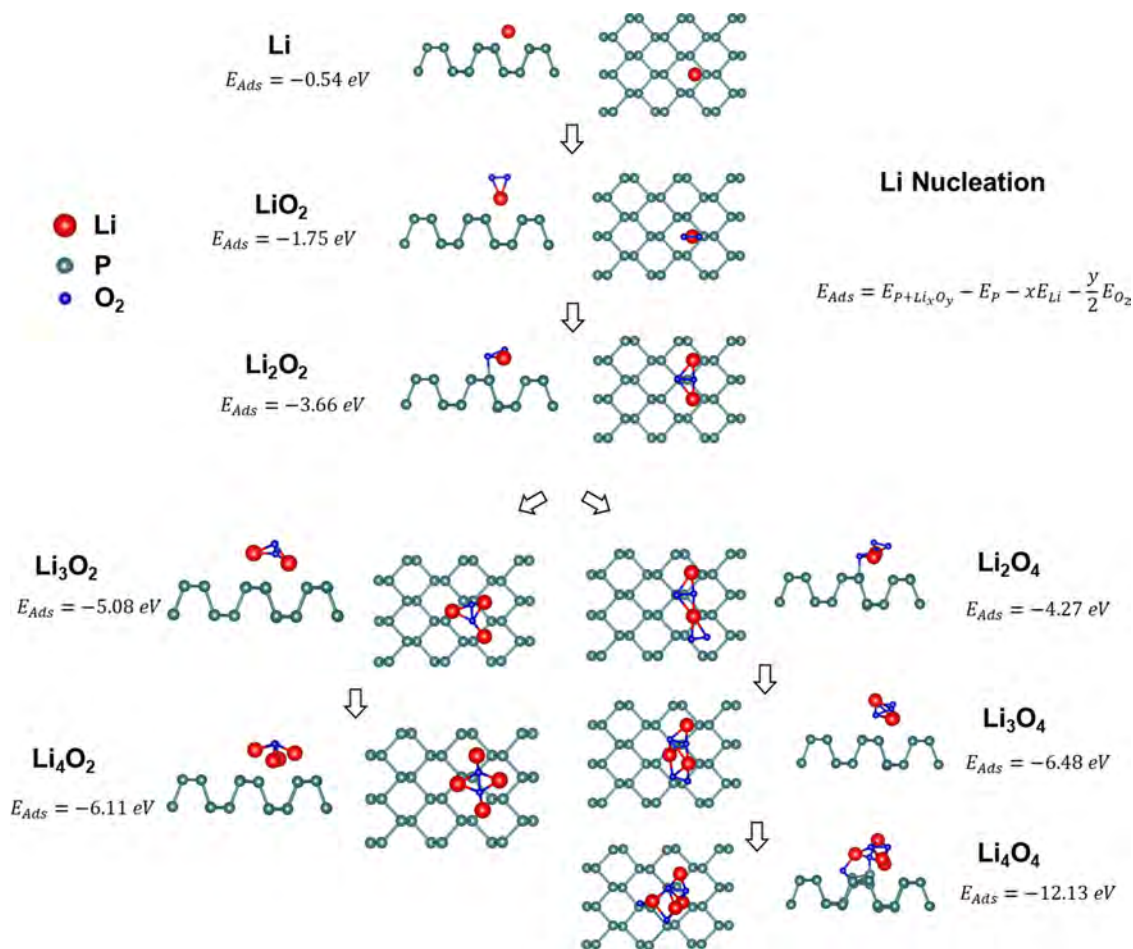


Figure 3. Optimized intermediate geometries of the reaction mechanism stemming from Li adsorption. Color code: green, P; blue, O; and red, Li. Atomic structures were visualized using VESTA.⁴⁵

side of the diamond from the tail in Li_3O_2 , creating a symmetric molecular structure. Consider now the alternate path that ends with Li_4O_4 . First, a second O_2 molecule was dissociated near Li_2O_2 to produce Li_2O_4 . As the additional O_2 molecule separated, it was observed to pull one of the Li atoms toward it, breaking the symmetry of the Li_2O_2 molecule. However, by comparing the bond angles of Li_2O_4 and Li_2O_2 , the dragged Li forms a bond angle of 97° between the newly dissociated O atoms, which is comparable to the bond angle of Li at the top of Li_2O_2 , with 96° . This periodicity may be an indicator of an ability to evenly coat the substrate with this discharge product. Building upon this idea of creating a periodic layer on the surface, the addition of another Li atom to obtain Li_3O_4 reproduced the diamondlike symmetry observed with Li_2O_2 (Figure 1). With the addition of another Li atom to form the second unit of Li_2O_2 , the symmetry is maintained.

3.1.2. Free-Energy Diagram from O_2 Nucleation. Using the formation energies and the vibrational calculations for each optimized intermediate, the Gibbs free energies at each step of the reaction mechanism were computed. Subsequently, two important parameters of phosphorene's theorized performance can be evaluated: the predicted final discharge product and ORR/OER overpotential. To predict the final discharge product, the difference in Gibbs free energies between the two final steps must be analyzed (see Figure 2a). From the mechanism described in Section 3.1.1, the reaction branches in two directions at Li_2O_2 , leading to a final product of either

Li_4O_4 or Li_4O_2 . We observed that dissociating O_2 to form Li_2O_4 is much more favorable than the addition of another Li, with the former yielding a change of -5.1 versus -0.4 eV for the latter. This is further confirmed by the continuing downhill nature of the path to Li_4O_4 with a more negative change in Gibbs free energy compared to that for the Li_4O_2 branch (difference of 7.1 eV between the final products). Keeping this in mind, we henceforth will only use the preferred path for subsequent analysis.

When a potential is applied, U , the change in the Gibbs free energy is augmented by $-neU$ ^{8,13,16} from the influence on the involved electrons at the electrode. We again plot the reaction mechanism with $U = 0$, but now with the final discharge product as the reference point (Figure 2b). From this path, the smallest and largest steps of the reaction may be identified. In this case, the largest step is from Li_2O_2 to Li_3O_4 of magnitude 6.62 eV and the smallest step is from LiO_2 to Li_2O_2 with a difference of 1.31 eV. Next, to calculate the equilibrium potential, which is the potential at which the initial step and the final step are equal in Gibbs free energy, the Nernst equation is applied as done previously^{9,15}

$$U_{\text{eq}} = \frac{-\Delta G_f^{\text{Li}_4\text{O}_4}}{ne} \quad (9)$$

where $\Delta G_f^{\text{Li}_4\text{O}_4} = G_{\text{Li}_4\text{O}_4} - 4G_{\text{Li}} - 2G_{\text{O}_2}$, n is the number of electrons transferred, and e is the elementary charge. Here, the

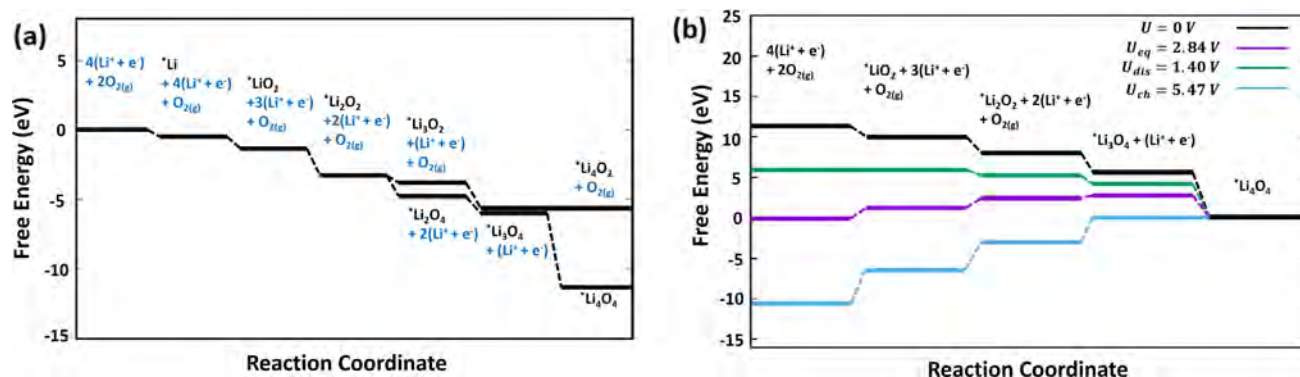


Figure 4. (a) Free-energy diagram comparing the two mechanism branches starting from Li nucleation and leading to either Li_4O_2 or Li_4O_4 . (b) Free-energy diagram illustrating the mechanism at different electric potentials.

equilibrium potential has been computed to be 3.79 V. The discharge potential of the reaction, which is the maximum voltage such that all intermediate steps are downhill, can also be calculated using the following relation⁶⁰

$$U_{\text{dis}} = \min \frac{-\Delta G_i}{e} \quad (10)$$

where ΔG_i is the change in Gibbs free energy between consecutive steps. In other words, any potential larger than this will cause this reaction step to become uphill. From the smallest step of LiO_2 to Li_2O_2 , a discharge potential of 1.31 V was computed. Taking this further, the overpotential of discharging is defined as $\eta_{\text{ORR}} \equiv U_{\text{eq}} - U_{\text{dis}}$, which will ideally be as low as possible to increase efficiency. Therefore, using phosphorene as a catalyst, the overpotential for ORR is predicted to be 2.48 V (from the O_2 nucleation path). We will now shift focus to the charging potential, which is the lowest potential that yields an entirely downhill OER mechanism going from right to left in Figure 2b. To calculate this voltage, a similar relation may be employed as that for ORR⁶⁰

$$U_{\text{ch}} = \max \frac{-\Delta G_i}{e} \quad (11)$$

By selecting the largest step in the mechanism, any potential lower than this will result in one of the steps being uphill when going from right to left. From the largest step of Li_2O_2 to Li_3O_4 , a charging potential of 6.62 V was calculated. Building upon this, the overpotential for charging can be calculated using $\eta_{\text{OER}} \equiv U_{\text{ch}} - U_{\text{eq}}$, giving a predicted value of 2.83 V (from the O_2 nucleating path).

3.1.3. Reaction Intermediate Geometries from Li Nucleation. In the same manner as for Section 3.1.1, we now consider the process stemming from Li adsorption with the geometries shown in Figure 3. This process is kinetically favored over the alternate path in Section 3.1.1 as it requires no activation energy. Therefore, from this kinetic reasoning, we argue that the mechanism starting from Li adsorption is the dominant reaction.

Starting from Li adsorption, the addition of an O_2 dimer leads to the formation of LiO_2 in a triangular shape, with both O atoms preferring to lie at the same height above the surface. This is in contrast to the predicted mechanism on $\delta\text{-MnO}_2$ where the addition of O_2 to adsorbed Li was found to orient itself such that the O_2 bond was perpendicular to the plane of the catalyst.¹⁶ We also considered the scenario where O_2 arrives first, but does not successfully dissociate, and a Li atom arrives. What we observed was that although Li can sit on top of the O_2 molecule it is a

higher energy state than that with Li at the bottom (-0.93 vs -1.75 eV). Additionally, and more importantly, we found that this configuration of Li on top is unstable because when we nudged the Li atom by 0.5 \AA , it swings below the O_2 to form the same LiO_2 configuration as when Li arrives first. Adsorbing an additional Li onto LiO_2 yielded a diamondlike structure comparable to that of the Li_2O_2 formed starting from O_2 dissociation. However, therein lies the difference in that this Li_2O_2 structure had the O_2 bond still intact at the center. Interestingly, this structure converged to a non-spin-polarized state, whereas the LiO_2 structure maintained the triplet spin orientation of the O_2 molecule, albeit weakened from the Li interaction. Building from Li_2O_2 is the branch point of the reaction, and the route leading to Li_4O_4 will be studied first. The initial step along this path from Li_2O_2 is to form Li_2O_4 because of the addition of O_2 . This additional O_2 molecule preferred to sit below the bottom Li of the diamond and orient itself parallel to the pre-existing O_2 in Li_2O_2 . This was the first indication of a larger-scale symmetry that may form with this alternating fashion vertically. Symmetry was then further developed in Li_3O_4 with the Li preferring to lie beside the pre-existing Li and in between the O_2 pairs. As the cluster reached its maximum concentration of Li_4O_4 , the symmetry previously seen was destroyed and one of the O_2 bonds broke. The dissociation of these molecules will release a significant amount of energy and affect the predicted overpotentials. Now considering the second branch leading to Li_4O_2 , the first step is the formation of Li_3O_2 from Li_2O_2 . What is observed is that the third Li atom rotated the Li_2O_2 diamond such that two of the Li atoms now lay in their preferred adsorption sites (H-site). With the addition of the last Li to make Li_4O_2 , a comparable structure to the corresponding step in the O_2 path was formed. However, the central O_2 bond remained unbroken in the final cluster of this path.

3.1.4. Free-Energy Diagram for Li Nucleation. With the new formation energies and configurations, the free-energy diagram depicting reaction paths leading to either Li_4O_2 or Li_4O_4 is shown in Figure 4a. Here, it can be observed that this reaction stemming from Li adsorption also promotes Li_4O_4 . Thus, regardless of whether the reaction proceeds via O_2 nucleation or Li nucleation, the favored discharge product of Li_2O_2 is expected to form on the surface of phosphorene. Following the Li_4O_4 path in Figure 4a, the steps were relatively uniform until the last Li atom is added. This sudden drop can be mainly attributed to the breakage of one of the O_2 bonds. The influence of this drop on other properties is twofold: it will raise the equilibrium potential and will also increase the charging potential (because it is the largest step), thereby altering the predicted overpotentials.

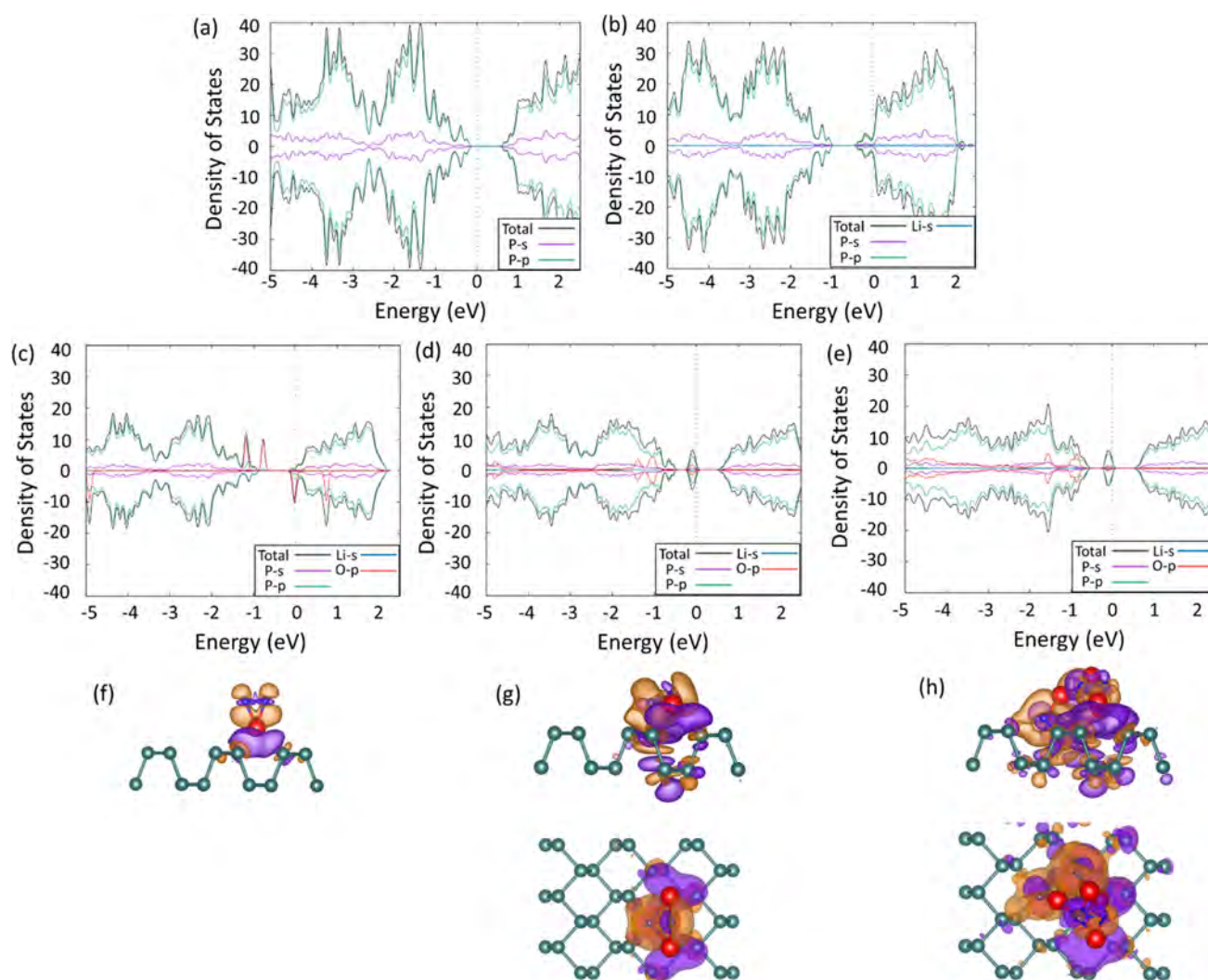


Figure 5. PDOS plots for (a) pristine phosphorene and (b) Li, (c) LiO_2 , (d) Li_2O_2 , and (e) Li_4O_4 on phosphorene. Spin-up is positive, and spin-down is negative. Differential charge density plots for (f) LiO_2 , (g) Li_2O_2 , and (h) Li_4O_4 on phosphorene. Purple shows charge accumulation, bronze shows charge depletion. Differential charge density plots were visualized using VESTA.⁴⁵

The equilibrium potential for this mechanism, computed using eq 9, was 2.84 V. This value is significantly closer to the experimental value of 2.96 V¹⁵ for Li_2O_2 than that in the O_2 nucleation mechanism (3.79 V), which bolsters the argument that this Li nucleation path is the more dominant of the two. The experimental value of the equilibrium potential is found by measurement of the formation energy of bulk Li_2O_2 at standard temperature and pressure along with the Nernst equation and is independent of the substrate employed. Moving onto the discharge potential, the limiting step is expected to be the initial LiO_2 formation because this step is smallest when no potential is applied. Applying eq 10 gave a discharge potential of magnitude 1.40 V. From this, we can then estimate the overpotential for discharge, which in this case was 1.44 V. Finally, the charge potential is limited by the final step of forming Li_4O_4 from Li_3O_4 , and its magnitude was predicted to be 5.47 V. Using this value to estimate the overpotential of the charging reaction gave an estimated value of 2.63 V. It is important to draw attention to how these overpotential values compare to those obtained from the alternate O_2 nucleation path. In both cases, the Li nucleation path was preferable with both overpotentials lower than their O_2 path counterparts. Because the Li nucleation path will be the

dominant reaction because of a lack of activation barrier, we consider these overpotentials as representative of the overall predicted catalytic performance of phosphorene.

3.1.5. Electronic Analysis of Intermediates. Shedding light on the electrical properties of the system as it undergoes the discharge reaction, Bader charge analysis⁴⁹ was performed and the PDOS and DCD plots for selected intermediates were generated (Figure 5). With the addition of a single Li atom to the lattice, a semiconductor-to-metal transition was observed as the Fermi Level is pulled into the conduction band. Essentially, Li n-dopes the system as it provides states in the conduction band and increases the number of electronic charge carriers (Figure 5b). Addition of an O_2 molecule to form LiO_2 maintained the metallic behavior as the Fermi energy remained in the conduction band (Figure 5c). The asymmetry between spin-up and spin-down in this plot stemmed from the O_2 bond that did not break upon adsorption, and the O p peaks (which show almost no hybridization) can be attributed to this bond. Using the DCD plot for this configuration to see how the charge of LiO_2 was redistributed due to phosphorene (Figure 5f), we see that the lattice pulled charge away from the Li–O bonds, as indicated via the charge depletion at these bonds and

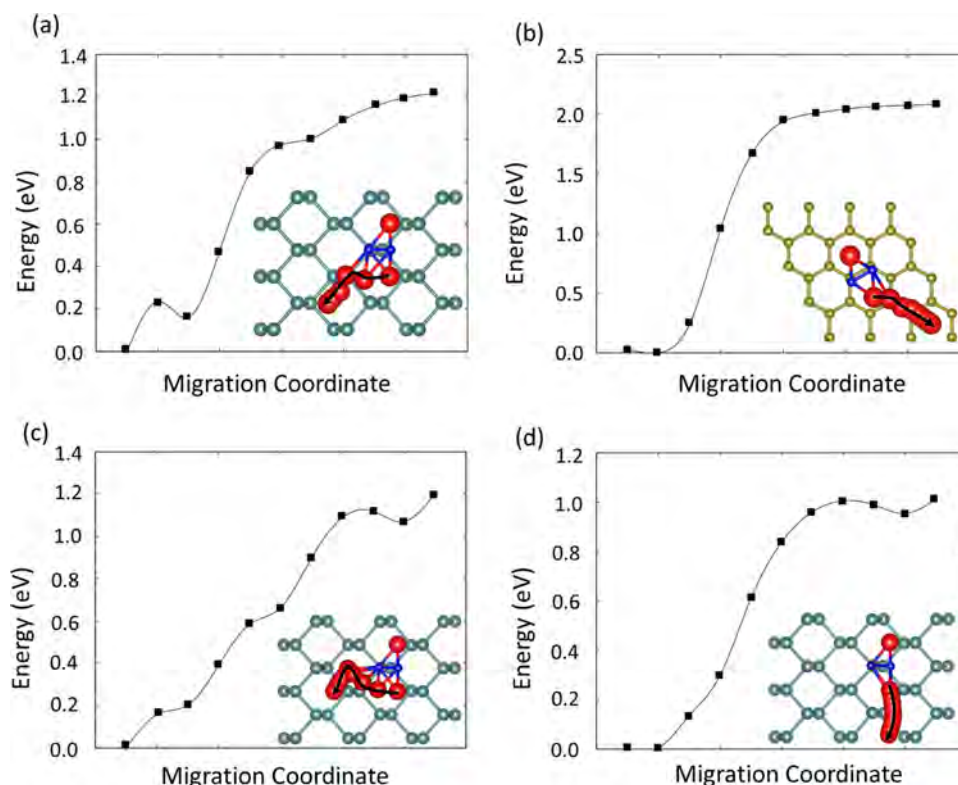


Figure 6. Energy profile for the removal of Li from Li_2O_2 on (a) phosphorene in a diagonal path, (b) graphene, (c) phosphorene along the armchair direction, and (d) phosphorene along the zigzag direction. Color code: green, P; blue, O; and red, Li. Atomic structures were visualized using VESTA.⁴⁵

accumulation between Li and phosphorene. This is verified through Bader analysis, which computed a relative charge of +0.88|e| for Li, where the three closest P atoms in the lattice gain on average 0.12|e|. Moving onto the next reaction step considered, Li_2O_2 , the system was no longer metallic as evidenced in the PDOS plot (Figure 5d) but instead was semiconducting. However, relative to that of the bare cathode (Figure 5a), the conductivity was improved as the band gap had reduced to approximately 0.4 eV. Drawing attention to the O p PDOS in this plot, more hybridization than in Li_2O_2 with P s and P p is observed. This hybridization is especially evident near the Fermi energy and at around -4 eV. This makes sense as looking at the geometric configuration of Li_2O_2 in Figure 3, the O atoms have been lowered in between the two Li atoms and lie closer to the phosphorene lattice. Moreover, DCD shows that the charge from Li is mainly pulled toward the substrate (Figure 5g), whereas Bader analysis reveals that the lithium atoms still give up 0.88|e|. Because the oxygen atoms are more electronegative than P and one of the O atoms can now directly interact with the substrate, O is expected to pull charge from the substrate. Bader corroborated this prediction by computing that the O atom closest to the surface gained 1.01|e| and the adjacent P atom lost 0.64|e|. The other O atom was not as close to the substrate and instead opted to interact with the surrounding two Li atoms. Continuing to the next considered product, Li_4O_4 , one of the oxygen bonds has broken at this stage. This presents itself in the PDOS plot via the observed hybridization between O-p, P-s, and P-p states (Figure 5e). Through Bader analysis, the nature of this bond breaking can be illuminated. With the additional Li atoms that were raised above the O atoms, they can now donate charge to the O atoms without phosphorene confiscating it. Additionally, the O atoms can still pull electrons from the lattice,

providing an additional source of charge. Therefore, with these two sources of charge, it was no longer favorable to form the double bond with the other nearest O and the bond breaks. Bader substantiated this claim through computing charges of $-1.91|e|$ and $-1.88|e|$ for each of the split O atoms, and the closest P atoms gave 1.45|e| and 1.64|e|, whereas all Li atoms gave an average of 0.89|e|. The second O pair did not split because the other lower Li atoms had their charge seized by the substrate, as shown in the DCD (Figure 5h), and blocked the direct interaction of O with the P atoms. In short, the source of the bond breaking is the difference in electronegativity with the cathode and the reconfiguration to allow the oxygen to interact with both the Li and P atoms without mutual interference. Also, PDOS illustrated that relative to that of pristine phosphorene the band gap of the final product was reduced and that, while on the path to this product, intermediates were expected to show metallic behavior.

4. CATALYTIC DECOMPOSITION OF Li_2O_2

Upon charging the system, the final discharge product of Li_4O_4 will be decomposed into its constituent atoms. In the case of aqueous electrolytes, redox mediators can be introduced to help this process,⁶¹ but here, we are considering a nonaqueous system, so another method of catalysis must be used. Previously, it has been shown experimentally that during charge of nonaqueous cells the Li–O bonds are broken, leaving Li vacancies,⁶² so a possible solution is if the catalyst material can also show activity toward this bond-breaking mechanism. Additionally, previous theoretical work has investigated bulk Li_2O_2 and has concluded that first Li vacancies form in the discharge product as it decomposes.⁶³ Ideally, the catalyst employed in the cathode will actively aid in this process, which

could be by providing minimal activation barriers for the breaking of Li–O bonds. For the removal of Li from Li_2O_2 on phosphorene, CI-NEB was used to find the minimum-energy pathway and activation barrier. The Li_2O_2 structure from the main Li adsorption path was used, and the first considered migration path will be diagonal along the lattice. We found that 1.22 eV is required to remove a Li atom from Li_2O_2 , which is visualized in Figure 6a. Note that only the migration of the separated Li atom is visualized here for clarity (Videos S1, S2, S3, S4 provide full animations of the decomposition processes described in the following sections). Giving the magnitude of this value greater context, we also considered graphene (with Li_2O_2 being formed via Li nucleation and the same procedure as for phosphorene). A 4×4 supercell (32 atoms) was used to keep the number of atoms approximately the same as for phosphorene and rule out any possible concentration effects. We found that on graphene the activation barrier for the removal of Li from Li_2O_2 is 2.06 eV, and the path is shown in Figure 6b.

From observation of the migration coordinate versus the energies of the obtained images, further details behind this bond breaking come to light. Starting with phosphorene (Figure 6a), as the dissociation process initiates from image 1 to 3, we see there is an initial barrier for the rotation of the Li_2O_2 molecule. The cause of orientation shift was the symmetry of the molecule requiring special placement on the surface to remove only one Li atom. From image 3 to image 7, we observe the bond breaking of Li–O, leaving separate Li and LiO_2 . From image 7 onward, the LiO_2 molecule rotated back to its initial position. Similarly, for graphene, there was an initial translation from 1 to 2, which was negligible in terms of energy difference (<0.05 eV), and from image 2 onward, the bond breaks as both LiO_2 moved toward their final positions.

Next, by splitting diffusion on phosphorene into the armchair and zigzag directions, the barriers along each path were isolated (Figure 6c,d). Starting with the armchair direction (Figure 6c), it began with a rotation of the full Li_2O_2 molecule until the fourth image. At this point, the Li–O bonds began to break as LiO_2 and Li moved to their final positions. Images 8 and 9 correspond to the isolated Li traversing the bridge site of the lattice. The total activation barrier along this path was 1.20 eV, which is very close to that of the diagonal path. Along the zigzag direction, as the Li got pulled toward its isolated final position, LiO_2 was rotated clockwise by one cell. In the final image, the LiO_2 remained in this rotated state, most likely due to the O atoms still seeing the charge from the separated Li, despite its broken bond. Image 8 corresponds again to the diffusion of the detached Li moving across the bridge site of the lattice into its final position. The activation barrier for this path was 1.01 eV, providing the lowest barrier observed. Therefore, phosphorene can catalytically contribute to the breaking of the Li–O bonds better than graphene, especially along the zigzag direction. Through the Arrhenius equation, $k \sim \exp\left(\frac{-E_A}{k_B T}\right)$, with k being the rate constant, E_A being the activation barrier, k_B being the Boltzmann constant, and T being the temperature (300 K), the difference in performance is emphasized as the kinetic rate constant of phosphorene will be approximately 10^{17} times greater than that of graphene.

To study whether the supercell size has any influence on these results, we also computed the minimum-energy pathway for different cells of both graphene and phosphorene with the results presented in Table S1. In the case of phosphorene, we considered 3×2 , 3×3 , and 3×4 , and for graphene, we

considered 4×4 , 4×5 , and 4×6 . For phosphorene, we observed that the lowest barrier was associated with the 3×3 supercell, whereas for the other two concentrations, the barriers observed were higher. This trend was not observed in graphene and could be a result of the different levels of substrate–Li interactions observed in phosphorene versus graphene and how the concentration influences these interactions.

Additionally, we also tested the effect of discharge product cluster size on these results by finding the activation barriers for removal of Li from Li_4O_4 . Here, we considered three possible decomposition mechanisms of removing Li atoms from the Li_4O_4 molecule (Figure S2). We have found that the barrier for the process shown in Figure S2c is the lowest observed, and it is for removing the bottommost Li in the structure. A possible explanation for this arises from Bader charge analysis of the Li_4O_4 structure. For the Li atom in question, it has the least positive charge in comparison to that of all other Li atoms (including those in Li_2O_2) with a charge of 0.86|e| in comparison to approximately 0.89|e| in all other cases. Therefore, the Li atom has the least interaction with its adjacent atoms and will require the least energy for removal. It can be concluded from this result that the size of the Li_xO_y cluster can influence the activation barrier for this decomposition process.

5. COMPARISON TO OTHER CATALYSTS

Before comparing the obtained overpotential predictions of phosphorene to those of other catalysts previously studied, it is important to note the effect of variation due to selection of computational parameters. As there is not a strict set of guidelines regarding the selection of computational parameters such as pseudopotentials and k -mesh density, the results found in Table 1 should not be taken too literally because the

Table 1. Theoretical ORR and OER Overpotentials of a Selection of Catalysts

catalyst	η_{ORR} (V)	η_{OER} (V)
phosphorene	1.44	2.63
silicene ¹³	1.39	4.09
h-BN/Ni(111) ¹⁴	1.15	0.74
GeS ¹¹	1.38	1.70
GeSe ¹¹	0.94	1.30
graphene ^{8,15}	1.25	2.16
N-doped graphene ¹⁵	0.89–1.66	
δ -MnO ₂ ¹⁶	1.21	0.49
Ni ₄ N ₃ (OH) ₂ ³⁹	0.18	
g-GeC ¹²	0.89	0.27
SL-SiC ⁹	0.73	2.60
g-SiC ₂ ⁹	0.85	2.20
g-SiC ₃ ⁹	1.86	4.61
Pd(111) ⁶⁴	0.56	1.66
PdCu(100) ⁶⁴	0.43	1.29
Pt(111) ⁵⁹	0.68	1.52
PtCu(111) ⁵⁹	0.26	0.49

nonuniformity of methodology will result in varying results. This section is intended to provide a qualitative estimate of phosphorene's performance relative to other catalysts through the identification of trends and patterns.

For a material to be considered an excellent catalyst, it must be able to facilitate very low overpotentials for both charging and discharging while also maintaining high capacity values and

diffusivity capabilities. The significance of overpotentials is that they reflect the round-trip efficiency of the battery employing this catalyst. It should be kept in mind that the magnitudes of the charge potential, discharge potential, and the overpotentials should not be directly compared to experimental values because they are dependent upon the current density.⁶⁵ Here, the overpotentials may be taken as a lower curb to experimental findings¹⁶ because the potentials considered are those of the limiting cases. Additionally, discrepancies between experimental and theoretical values could exist because of factors such as electrolytic influence and thermal vibrations. The electrolyte chosen can play a large role in deciding whether the reaction will proceed via the surface mechanism or a solution mechanism, thus affecting not only the path but also the morphology of the discharge product. Moreover, the electrolyte could further have an influence on charge transfer because of its dielectric properties. Considering now thermal vibrations, here, we used the harmonic approximation to estimate ZPE and the entropy. However, any anharmonic effects that may exist in the system are not captured via this approximation, leading to the opportunity for discrepancy. For these reasons, we will compare the theoretical values of a selection of 2D catalyst materials. Staying consistent with experimental findings, Pt and Pd are predicted to have some of the lowest overpotentials. Moreover, these precious metals perform even better when mounted on Cu. Thus, these materials are considered the benchmark to beat. However, these precious metals are predicted to promote the discharge product $2(\text{Li}_2\text{O})$,⁵⁹ which is not favored in terms of reversibility. Additionally, these precious metals are highly expensive and are therefore not viable options when considering a long-term scaling up of Li–air batteries.

While it becomes apparent that g-GeC gives the best balanced predicted values of those investigated so far, it still has its shortcomings. Namely, it promotes $2(\text{Li}_2\text{O})$ again¹² and also contains carbon, which should be avoided because of side reactions. The same carbon argument applies to all of the siligraphenes, which immediately adds a caveat to their predicted overpotentials. Moreover, with germanium's heaviness, the specific capacity of the cell will be restricted. This becomes evident when studying GeS for Li-ion batteries where it is predicted to have a specific capacity of only 256 mAh g^{-1} .^{66,67} Similarly, despite its low discharge overpotential, $\text{Ni}_4\text{N}_3(\text{OH})_2$'s weight will be detrimental to its capacity and further judgment must be held until its charging properties are studied. When placed in the context of phosphorene's anticipated specific capacity of 865 mAh g^{-1} for Li-ion batteries,⁶⁸ it becomes evident that phosphorene's lower weight is highly beneficial. Extrapolating this weight argument, the same can be said for most of the catalyst candidates in Table 1, which implement heavy materials such as selenium, manganese, and germanium. To highlight this point, 2D MnO_2 is predicted to have a capacity of 616 mAh g^{-1} ⁶⁹ and GeSe is predicted to have a capacity of 178 mAh g^{-1} .⁶⁷ The only materials in Table 1 exempt from this weight criticism that are also carbon-free are silicene and phosphorene. However, silicene is predicted to exhibit a high charging overpotential (4.09 V^{13}), much larger than that of phosphorene (2.63 V). Homing in on graphene, it does yield marginally better predicted overpotentials for both discharge and charge than phosphorene, despite its larger energy barrier for Li_2O_2 decomposition. First this may seem contradictory, but because overpotentials rely on a multitude of factors, smaller energy barriers do not guarantee better overpotentials but could certainly help lead to this outcome. However, again, the carbon

side reactions cannot be ignored and will play a role in practical investigations.

Another factor that cannot be ignored is the diffusive capabilities of Li on the substrate, which will provide an estimate of the catalyst's ability to form a uniform discharge product at an efficient rate. Previous studies into the suitability of phosphorene for Li-ion batteries revealed that Li needs to overcome an activation barrier of only 0.08 eV in the zigzag direction.⁷⁰ For context, it was found that Li diffusion on the surface of GeS, GeSe, and 2D MnO_2 requires surpassing a barrier of 0.236 eV^{66} (elsewhere given as 0.19 eV^{67}), 0.26 eV^{67} , and 0.148 eV^{69} respectively. As a result, we expect phosphorene to be able to formulate a much more uniform discharge product layer at a faster rate than its previously investigated competitors. Referring back to Section 4, the low activation barriers for decomposition, which are enabled by phosphorene, could increase the efficiency of the decomposition of the discharge products.

6. CONCLUSIONS

First-principles methods were employed to investigate phosphorene's capability for catalysis in the cathode of Li–air batteries. Reaction paths stemming from either O_2 dissociation or Li adsorption are explored, with the latter argued to be the dominant reaction and both expected to promote Li_2O_2 growth. The overpotentials from this dominant mechanism are computed to be 1.44 V for discharge and 2.63 V for charge. Also, the activation barrier for decomposition of the discharge products is found to be 1.01 eV for phosphorene, considerably lower than that of graphene and yielding a difference of 10^{17} in kinetic rate constants. Taking all results into consideration, phosphorene shows excellent potential as a catalyst in Li–air batteries.

■ ASSOCIATED CONTENT

📄 Supporting Information

The Supporting Information is available free of charge on the ACS Publications website at DOI: [10.1021/acsami.8b13505](https://doi.org/10.1021/acsami.8b13505).

Convergence test for vibrational analysis; supercell size influence on Li_2O_2 decomposition barrier; and decomposition barriers for Li_4O_4 (PDF)

Videos providing full animations of the Li_2O_2 decomposition processes described in the text (AVI) (AVI) (AVI) (AVI)

■ AUTHOR INFORMATION

Corresponding Author

*E-mail: chandraveer.singh@utoronto.ca.

ORCID

Lance Kavalsky: [0000-0002-7875-5652](https://orcid.org/0000-0002-7875-5652)

Sankha Mukherjee: [0000-0001-9094-0538](https://orcid.org/0000-0001-9094-0538)

Chandra Veer Singh: [0000-0002-6644-0178](https://orcid.org/0000-0002-6644-0178)

Notes

The authors declare no competing financial interest.

■ ACKNOWLEDGMENTS

The authors acknowledge funding by the Natural Sciences and Engineering Research Council of Canada (NSERC) through the Discovery grant, the Hart Professorship, and the University of Toronto. Compute Canada is also acknowledged for providing

computing resources at the SciNet CalculQuebec and Westgrid consortia.

REFERENCES

- (1) Tan, P.; Jiang, H. R.; Zhu, X. B.; An, L.; Jung, C. Y.; Wu, M. C.; Shi, L.; Shyy, W.; Zhao, T. S. Advances and Challenges in Lithium-Air Batteries. *Appl. Energy* **2017**, *204*, 780–806.
- (2) Vegge, T.; Garcia-lastra, J. M.; Siegel, D. J. Lithium – Oxygen Batteries: At a Crossroads? *Curr. Opin. Electrochem.* **2017**, *6*, 100–107.
- (3) Abraham, K. M.; Jiang, Z. A Polymer Electrolyte – Based Rechargeable Lithium / Oxygen Battery. *J. Electrochem. Soc.* **1996**, *143*, 1–5.
- (4) Radin, M. D.; Rodriguez, J. F.; Tian, F.; Siegel, D. J. Lithium Peroxide Surfaces Are Metallic, While Lithium Oxide Surfaces Are Not. *J. Am. Chem. Soc.* **2012**, *134*, 1093–1102.
- (5) Surya, K.; Michael, M. S.; Prabakaran, S. R. S. A Review on Advancement in Non-Noble Metal Based Oxides as Bifunctional Catalysts for Rechargeable Non-Aqueous Li/Air Battery. *Solid State Ionics* **2018**, *317*, 89–96.
- (6) Débart, A.; Bao, J.; Armstrong, G.; Bruce, P. G. An O₂ Cathode for Rechargeable Lithium Batteries: The Effect of a Catalyst. *J. Power Sources* **2007**, *174*, 1177–1182.
- (7) Lu, Y. C.; Gasteiger, H. A.; Shao-Horn, Y. Catalytic Activity Trends of Oxygen Reduction Reaction for Nonaqueous Li-air battery Batteries. *J. Am. Chem. Soc.* **2011**, *133*, 19048–19051.
- (8) Jiang, H. R.; Zhao, T. S.; Shi, L.; Tan, P.; An, L. First-Principles Study of Nitrogen-, Boron-Doped Graphene and Co-Doped Graphene as the Potential Catalysts in Nonaqueous Li-O₂Batteries. *J. Phys. Chem. C* **2016**, *120*, 6612–6618.
- (9) Dong, H.; Ji, Y.; Hou, T.; Li, Y. Two-Dimensional Siligraphenes as Cathode Catalysts for Nonaqueous Lithium-Oxygen Batteries. *Carbon* **2018**, *126*, 580–587.
- (10) Ottakam Thotiyil, M. M.; Freunberger, S. A.; Peng, Z.; Bruce, P. G. The Carbon Electrode in Nonaqueous Li-O₂ Cells. *J. Am. Chem. Soc.* **2013**, *135*, 494–500.
- (11) Ji, Y.; Dong, H.; Yang, M.; Hou, T.; Li, Y. Monolayer Germanium Monochalcogenides (GeS/GeSe) as Cathode Catalysts in Nonaqueous Li–O₂ Batteries. *Phys. Chem. Chem. Phys.* **2017**, *19*, 20457–20462.
- (12) Ji, Y.; Dong, H.; Hou, T.; Li, Y. Monolayer Graphitic Germanium Carbide (g-GeC): The Promising Cathode Catalysts for Fuel Cell and Lithium-Oxygen Battery Applications. *J. Mater. Chem. A* **2018**, *6*, 2212–2218.
- (13) Hwang, Y.; Yun, K. H.; Chung, Y. C. Carbon-Free and Two-Dimensional Cathode Structure Based on Silicene for Lithium-Oxygen Batteries: A First-Principles Calculation. *J. Power Sources* **2015**, *275*, 32–37.
- (14) Lee, M.; Hwang, Y.; Yun, K. H.; Chung, Y. C. Cathode Reaction Mechanism on the H-BN/Ni (111) Heterostructure for the Lithium-Oxygen Battery. *J. Power Sources* **2016**, *307*, 379–384.
- (15) Jing, Y.; Zhou, Z. Computational Insights into Oxygen Reduction Reaction and Initial Li₂O₂ Nucleation on Pristine and N-Doped Graphene in Li-O₂ Batteries. *ACS Catal.* **2015**, *5*, 4309–4317.
- (16) Liu, Z.; De Jesus, L. R.; Banerjee, S.; Mukherjee, P. P. Mechanistic Evaluation of Li_xO_y Formation on δ -MnO₂ in Nonaqueous Li-Air Batteries. *ACS Appl. Mater. Interfaces* **2016**, *8*, 23028–23036.
- (17) Ren, W.; Zhang, H.; Guan, C.; Cheng, C. Ultrathin MoS₂Nanosheets@Metal Organic Framework-Derived N-Doped Carbon Nanowall Arrays as Sodium Ion Battery Anode with Superior Cycling Life and Rate Capability. *Adv. Funct. Mater.* **2017**, *27*, No. 1702116.
- (18) Sun, J.; Lee, H. W.; Pasta, M.; Yuan, H.; Zheng, G.; Sun, Y.; Li, Y.; Cui, Y. A Phosphorene-Graphene Hybrid Material as a High-Capacity Anode for Sodium-Ion Batteries. *Nat. Nanotechnol.* **2015**, *10*, 980–985.
- (19) Cha, E.; Patel, M. D.; Park, J.; Hwang, J.; Prasad, V.; Cho, K.; Choi, W. 2D MoS₂ as an Efficient Protective Layer for Lithium Metal Anodes in High-Performance Li–S Batteries. *Nat. Nanotechnol.* **2018**, *13*, 337–344.
- (20) Mukherjee, S.; Kavalsky, L.; Singh, C. V. Ultrahigh Storage and Fast Diffusion of Na and K in Blue Phosphorene Anodes. *ACS Appl. Mater. Interfaces* **2018**, *10*, 8630–8639.
- (21) Li, L.; Chen, L.; Mukherjee, S.; Gao, J.; Sun, H.; Liu, Z.; Ma, X.; Gupta, T.; Singh, C. V.; Ren, W.; Cheng, H. M.; Koratkar, N. Phosphorene as a Polysulfide Immobilizer and Catalyst in High-Performance Lithium–Sulfur Batteries. *Adv. Mater.* **2017**, *29*, No. 1602734.
- (22) Wu, S.; Hui, K. S.; Hui, K. N. 2D Black Phosphorus: From Preparation to Applications for Electrochemical Energy Storage. *Adv. Sci.* **2018**, *5*, No. 1700491.
- (23) Jain, R.; Narayan, R.; Sasikala, S. P.; Lee, K. E.; Jung, H. J.; Kim, S. O. Phosphorene for Energy and Catalytic Application—filling the Gap between Graphene and 2D Metal Chalcogenides. *2D Mater.* **2017**, *4*, No. 042006.
- (24) Walia, S.; Sabri, Y.; Ahmed, T.; Field, M. R.; Ramanathan, R.; Arash, A.; Bhargava, S. K.; Sriram, S.; Bhaskaran, M.; Bansal, V.; Balendhran, S. Defining the Role of Humidity in the Ambient Degradation of Few-Layer Black Phosphorus. *2D Mater.* **2017**, *4*, No. 015025.
- (25) Favron, A.; Gauffrès, E.; Fossard, F.; Phaneuf-Laheureux, A. L.; Tang, N. Y. W.; Lévesque, P. L.; Loiseau, A.; Leonelli, R.; Francoeur, S.; Martel, R. Photooxidation and Quantum Confinement Effects in Exfoliated Black Phosphorus. *Nat. Mater.* **2015**, *14*, 826–832.
- (26) Ahmed, T.; Balendhran, S.; Karim, M. N.; Mayes, E. L. H.; Field, M. R.; Ramanathan, R.; Singh, M.; Bansal, V.; Sriram, S.; Bhaskaran, M.; Walia, S. Degradation of Black Phosphorus Is Contingent on UV–blue Light Exposure. *npj 2D Mater. Appl.* **2017**, *1*, No. 18.
- (27) Wang, G.; Slough, W. J.; Pandey, R.; Karna, S. P. Degradation of Phosphorene in Air: Understanding at Atomic Level. *2D Mater.* **2016**, *3*, No. 025011.
- (28) Farooqui, U. R.; Ahmad, A. L.; Hamid, N. A. Challenges and Potential Advantages of Membranes in Lithium Air Batteries: A Review. *Renewable Sustainable Energy Rev.* **2017**, *77*, 1114–1129.
- (29) Liu, Y.; Wang, L.; Cao, L.; Shang, C.; Wang, Z.; Wang, H.; He, L.; Yang, J.; Cheng, H.; Li, J.; Lu, Z. Understanding and Suppressing Side Reactions in Li–air Batteries. *Mater. Chem. Front.* **2017**, *1*, 2495–2510.
- (30) Elbadawi, C.; Queralt, R. T.; Xu, Z. Q.; Bishop, J.; Ahmed, T.; Kuriakose, S.; Walia, S.; Toth, M.; Aharonovich, I.; Lobo, C. J. Encapsulation-Free Stabilization of Few-Layer Black Phosphorus. *ACS Appl. Mater. Interfaces* **2018**, *10*, 24327–24331.
- (31) Pei, J.; Gai, X.; Yang, J.; Wang, X.; Yu, Z.; Choi, D. Y.; Luther-Davies, B.; Lu, Y. Producing Air-Stable Monolayers of Phosphorene and Their Defect Engineering. *Nat. Commun.* **2016**, *7*, No. 10450.
- (32) Kim, J. S.; Liu, Y.; Zhu, W.; Kim, S.; Wu, D.; Tao, L.; Dodabalapur, A.; Lai, K.; Akinwande, D. Toward Air-Stable Multilayer Phosphorene Thin-Films and Transistors. *Sci. Rep.* **2015**, *5*, No. 8989.
- (33) Chen, L.; Zhou, G.; Liu, Z.; Ma, X.; Chen, J.; Zhang, Z.; Ma, X.; Li, F.; Cheng, H. M.; Ren, W. Scalable Clean Exfoliation of High-Quality Few-Layer Black Phosphorus for a Flexible Lithium Ion Battery. *Adv. Mater.* **2016**, *28*, 510–517.
- (34) Batmunkh, M.; Shrestha, A.; Bat-Erdene, M.; Nine, M. J.; Shearer, C. J.; Gibson, C.; Slattery, A.; Tawfik, S.; Ford, M.; Dai, S.; Qiao, S.; Shapter, J. G. Electrocatalytic Activity of 2D Phosphorene Based Heteroelectrocatalyst for Photoelectrochemical Cells. *Angew. Chem., Int. Ed.* **2018**, *57*, 2644–2647.
- (35) Ren, X.; Zhou, J.; Qi, X.; Liu, Y.; Huang, Z.; Li, Z.; Ge, Y.; Dhanabalan, S. C.; Ponraj, J. S.; Wang, S.; Zhong, J.; Zhang, H. Few-Layer Black Phosphorus Nanosheets as Electrocatalysts for Highly Efficient Oxygen Evolution Reaction. *Adv. Energy Mater.* **2017**, *7*, No. 1700396.
- (36) Lyu, Z.; Zhou, Y.; Dai, W.; Cui, X.; Lai, M.; Wang, L.; Huo, F.; Huang, W.; Hu, Z.; Chen, W. Recent Advances in Understanding of the Mechanism and Control of Li₂O₂ Formation in Aprotic Li–O₂ Batteries. *Chem. Soc. Rev.* **2017**, *46*, 6046–6072.
- (37) Ma, L.; Yu, T.; Tzoganakis, E.; Amine, K.; Wu, T.; Chen, Z.; Lu, J. Fundamental Understanding and Material Challenges in Rechargeable Nonaqueous Li–O₂Batteries: Recent Progress and Perspective. *Adv. Energy Mater.* **2018**, *8*, No. 1800348.

- (38) Lim, H.-D.; Lee, B.; Bae, Y.; Park, H.; Ko, Y.; Kim, H.; Kim, J.; Kang, K. Reaction Chemistry in Rechargeable Li–O₂ Batteries. *Chem. Soc. Rev.* **2017**, *46*, 2873–2888.
- (39) Lee, A.; Krishnamurthy, D.; Viswanathan, V. Exploring MXenes as Cathodes for Non-Aqueous Lithium–Oxygen Batteries: Design Rules for Selectively Nucleating Li₂O₂. *ChemSusChem* **2018**, *11*, 1911–1918.
- (40) Yilmaz, E.; Yogi, C.; Yamanaka, K.; Ohta, T.; Byon, H. R. Promoting Formation of Noncrystalline Li₂O₂ in the Li–O₂ Battery with RuO₂ Nanoparticles. *Nano Lett.* **2013**, *13*, 4679–4684.
- (41) Giannozzi, P.; Baroni, S.; Bonini, N.; Calandra, M.; Car, R.; Cavazzoni, C.; Ceresoli, D.; Chiarotti, G. L.; Cococcioni, M.; Dabo, I.; Dal Corso, A.; De Gironcoli, S.; Fabris, S.; Fratesi, G.; Gebauer, R.; Gerstmann, U.; Gougousis, C.; Kokalj, A.; Lazzeri, M.; Martin-Samos, L.; Marzari, N.; Mauri, F.; Mazzarello, R.; Paolini, S.; Pasquarello, A.; Paulatto, L.; Sbraccia, C.; Scandolo, S.; Sclauzero, G.; Seitsonen, A. P.; Smogunov, A.; Umari, P.; Wentzcovitch, R. M. QUANTUM ESPRESSO: A Modular and Open-Source Software Project for Quantum Simulations of Materials. *J. Phys. Condens. Matter* **2009**, *21*, No. 395502.
- (42) Blöchl, P. E. Projector Augmented-Wave Method. *Phys. Rev. B* **1994**, *50*, 17953–17979.
- (43) Perdew, J. P.; Burke, K.; Ernzerhof, M. Generalized Gradient Approximation Made Simple. *Phys. Rev. Lett.* **1996**, *77*, 3865–3868.
- (44) Barone, V.; Casarin, M.; Forrer, D.; Pavone, M.; Sambri, M.; Vittadini, A. Role and Effective Treatment of Dispersive Forces in Materials: Polyethylene and Graphite Crystals as Test Cases. *J. Comput. Chem.* **2009**, *30*, 934–939.
- (45) Momma, K.; Izumi, F. VESTA 3 for Three-Dimensional Visualization of Crystal, Volumetric and Morphology Data. *J. Appl. Crystallogr.* **2011**, *44*, 1272–1276.
- (46) Monkhorst, H.; Pack, J. Special Points for Brillouin Zone Integrations. *Phys. Rev. B* **1976**, *13*, 5188–5192.
- (47) Fletcher, R. A New Approach to Variable Metric Algorithms. *Comput. J.* **1970**, *13*, 317–322.
- (48) Ziletti, A.; Carvalho, A.; Campbell, D. K.; Coker, D. F.; Castro Neto, A. H. Oxygen Defects in Phosphorene. *Phys. Rev. Lett.* **2015**, *114*, No. 046801.
- (49) Tang, W.; Sanville, E.; Henkelman, G. A Grid-Based Bader Analysis Algorithm without Lattice Bias. *J. Phys. Condens. Matter* **2009**, *21*, No. 084204.
- (50) Reuter, K.; Scheffler, M. Composition, Structure and Stability of RuO₂(110) as a Function of Oxygen Pressure. *Phys. Rev. B* **2001**, *65*, No. 035406.
- (51) Soon, A.; Todorova, M.; Delley, B.; Stampfl, C. Thermodynamic Stability and Structure of Copper Oxide Surfaces: A First-Principles Investigation. *Phys. Rev. B* **2007**, *75*, No. 125420.
- (52) Hjorth Larsen, A.; Jørgen Mortensen, J.; Blomqvist, J.; Castelli, I. E.; Christensen, R.; Dulak, M.; Friis, J.; Groves, M. N.; Hammer, B.; Hargus, C.; Hermes, E. D.; Jennings, P. C.; Bjerre Jensen, P.; Kermode, J.; Kitchin, J. R.; Leonhard Kolsbjerg, E.; Kubal, J.; Kaasbjerg, K.; Lysgaard, S.; Bergmann Maronsson, J.; Maxson, T.; Olsen, T.; Pastewka, L.; Peterson, A.; Rostgaard, C.; Schiøtz, J.; Schütt, O.; Strange, M.; Thygesen, K. S.; Vegge, T.; Vilhelmsen, L.; Walter, M.; Zeng, Z.; Jacobsen, K. W. The Atomic Simulation Environment - A Python Library for Working with Atoms. *J. Phys.: Condens. Matter* **2017**, *29*, No. 273002.
- (53) Henkelman, G.; Uberuaga, B. P.; Jónsson, H. Climbing Image Nudged Elastic Band Method for Finding Saddle Points and Minimum Energy Paths. *J. Chem. Phys.* **2000**, *113*, 9901–9904.
- (54) Zhou, G.; Tian, H.; Jin, Y.; Tao, X.; Liu, B.; Zhang, R.; Seh, Z. W.; Zhuo, D.; Liu, Y.; Sun, J.; Zhao, J.; Zu, C.; Wu, D. S.; Zhang, Q.; Cui, Y. Catalytic Oxidation of Li₂S on the Surface of Metal Sulfides for Li–S Batteries. *Proc. Natl. Acad. Sci. USA* **2017**, *114*, 840–845.
- (55) Kulish, V. V.; Malyi, O. I.; Persson, C.; Wu, P. Adsorption of Metal Adatoms on Single-Layer Phosphorene. *Phys. Chem. Chem. Phys.* **2015**, *17*, 992–1000.
- (56) Hu, T.; Hong, J. First-Principles Study of Metal Adatom Adsorption on Black Phosphorene. *J. Phys. Chem. C* **2015**, *119*, 8199–8207.
- (57) Guo, G.-C.; Wei, X.-L.; Wang, D.; Luo, Y.; Liu, L.-M. Pristine and Defect-Containing Phosphorene as Promising Anode Materials for Rechargeable Li Batteries. *J. Mater. Chem. A* **2015**, *3*, 11246–11252.
- (58) Orellana, W.; da Silva, A. J. R.; Fazzio, A. Oxidation at the Si/SiO₂ Interface: Influence of the Spin Degree of Freedom. *Phys. Rev. Lett.* **2003**, *90*, No. 016103.
- (59) Lee, M.; Hwang, Y.; Yun, K.; Chung, Y. Greatly Improved Electrochemical Performance of Lithium–Oxygen Batteries with a Bimetallic Platinum–Copper Alloy Catalyst. *J. Power Sources* **2015**, *288*, 296–301.
- (60) Hummelshøj, J. S.; Blomqvist, J.; Datta, S.; Vegge, T.; Rossmeisl, J.; Thygesen, K. S.; Luntz, A. C.; Jacobsen, K. W.; Nørskov, J. K. Communications: Elementary Oxygen Electrode Reactions in the Aprotic Li–Air Battery. *J. Chem. Phys.* **2010**, *132*, No. 071101.
- (61) Aurbach, D.; McCloskey, B. D.; Nazar, L. F.; Bruce, P. G. Advances in Understanding Mechanisms Underpinning Lithium–Air Batteries. *Nat. Energy* **2016**, *1*, No. 16128.
- (62) Ganapathy, S.; Adams, B. D.; Stenou, G.; Anastasaki, M. S.; Goubitz, K.; Miao, X.-F.; Nazar, L. F.; Wagemaker, M. Nature of Li₂O₂ Oxidation in a Li–O₂ Battery Revealed by Operando X-Ray Diffraction. *J. Am. Chem. Soc.* **2014**, *136*, 16335–16344.
- (63) Kang, S.; Mo, Y.; Ong, S. P.; Ceder, G. A Facile Mechanism for Recharging Li₂O₂ in Li–O₂ Batteries. *Chem. Mater.* **2013**, *25*, 3328–3336.
- (64) Choi, R.; Jung, J.; Kim, G.; Song, K.; Kim, Y.-I.; Jung, S. C.; Han, Y.-K.; Song, H.; Kang, Y.-M. Ultra-Low Overpotential and High Rate Capability in Li–O₂ Batteries through Surface Atom Arrangement of PdCu Nanocatalysts. *Energy Environ. Sci.* **2014**, *7*, 1362–1368.
- (65) Kulkarni, A.; Siahrostami, S.; Patel, A.; Nørskov, J. K. Understanding Catalytic Activity Trends in the Oxygen Reduction Reaction. *Chem. Rev.* **2018**, *118*, 2302–2312.
- (66) Li, F.; Qu, Y.; Zhao, M. Germanium Sulfide Nanosheet: A Universal Anode Material for Alkali Metal Ion Batteries. *J. Mater. Chem. A* **2016**, *4*, 8905–8912.
- (67) Zhou, Y. MX (M = Ge, Sn; X = S, Se) Sheets: Theoretical Prediction of New Promising Electrode Materials for Li Ion Batteries. *J. Mater. Chem. A* **2016**, *4*, 10906–10913.
- (68) Zhang, C.; Yu, M.; Anderson, G.; Dharmasena, R. R.; Sumanasekera, G. The Prospects of Phosphorene as an Anode Material for High-Performance Lithium-Ion Batteries: A Fundamental Study. *Nanotechnology* **2017**, *28*, No. 075401.
- (69) Deng, S.; Wang, L.; Hou, T.; Li, Y. Two-Dimensional MnO₂ as a Better Cathode Material for Lithium Ion Batteries. *J. Phys. Chem. C* **2015**, *119*, 28783–28788.
- (70) Li, W.; Yang, Y.; Zhang, G.; Zhang, Y. W. Ultrafast and Directional Diffusion of Lithium in Phosphorene for High-Performance Lithium-Ion Battery. *Nano Lett.* **2015**, *15*, 1691–1697.